The Astrophysical Journal Letters, 987:L31 (10pp), 2025 July 10 https://doi.org/10.3847/2041-8213/ade680

Optical+Near-IR Analysis of a Newly Confirmed Einstein Ring at $z \sim 1$ from the Kilo-Degree Survey: Dark Matter Fraction, Total and Dark Matter Density Slope, and Initial Mass Function*

Rui Li[1], Nicola R. Napolitano[2,3,4], Giuseppe D'Ago[5], Vyacheslav N. Shalyapin[6,7], Kai Zhu[8], Xiaotong Guo[9], Ran Li[10,11], Léon V. E. Koopmans[12], Chiara Spiniello[13,14], Crescenzo Tortora[14], Francesco La Barbera[14], Haicheng Feng[15], Liang Gao[10,1], Zhiqi Huang[3], Koen Kuijken[16], Hui Li[1], Linghua Xie[3], Mario Radovich[17], and Alexey Sergeyev[18,19,20]
[1] Institute for Astrophysics, School of Physics, Zhengzhou University, Zhengzhou, 450001, People's Republic of China; liruiww@gmail.com
[2] Department of Physics "E. Pancini," University Federico II, Via Cinthia 6, 80126-I, Naples, Italy; nicolarosario.napolitano@unina.it
[3] School of Physics and Astronomy, Sun Yat-sen University, Zhuhai Campus, 2 Daxue Road, Xiangzhou District, Zhuhai, People's Republic of China
[4] CSST Science Center for Guangdong-Hong Kong-Macau Great Bay Area, Zhuhai, 519082, People's Republic of China
[5] Institute of Astronomy, University of Cambridge, Madingley Road, Cambridge, CB3 0HA, UK
[6] Departamento de Fí sica Moderna, Universidad de Cantabria, Avda. de Los Castros s/n, E-39005 Santander, Spain
[7] O.Ya. Usikov Institute for Radiophysics and Electronics, National Academy of Sciences of Ukraine, 12 Acad. Proscury St., UA-61085 Kharkiv, Ukraine
[8] Department of Astronomy, Tsinghua University, Beijing 100084, People's Republic of China
[9] Institute of Astronomy and Astrophysics, Anqing Normal University, Anqing, Anhui 246133, People's Republic of China
[10] School of Physics and Astronomy, Beijing Normal University, Beijing 100875, People's Republic of China
[11] School of Astronomy and Space Science, University of Chinese Academy of Science, Beijing 100049, People's Republic of China
[12] Kapteyn Astronomical Institute, University of Groningen, P.O.Box 800, 9700AV Groningen, The Netherlands
[13] Department of Physics, University of Oxford, Denys Wilkinson Building, Keble Road, Oxford OX1 3RH, UK
[14] INAF—Osservatorio Astronomico di Capodimonte, Salita Moiariello 16, 80131—Napoli, Italy
[15] Yunnan Observatories, Chinese Academy of Sciences, Kunming, 650011, Yunnan, People's Republic of China
[16] Leiden Observatory, Leiden University, P.O.Box 9513, 2300RA Leiden, The Netherlands
[17] INAF—Osservatorio Astronomico di Padova, via dell'Osservatorio 5, 35122 Padova, Italy
[18] Université Côte d'Azur, Observatoire de la Côte d'Azur, CNRS, Laboratoire Lagrange, France
[19] V. N. Karazin Kharkiv National University, Kharkiv, 61022, Ukraine
[20] Institute of Radio Astronomy of National Academy of Science of Ukraine, Mystetstv 4, Ukraine
Received 2025 March 24; revised 2025 June 17; accepted 2025 June 17; published 2025 July 4

Abstract

We report the spectroscopic confirmation of a bright blue Einstein ring in the Kilo-Degree Survey (KiDS) footprint: the Einstein "blue eye." Spectroscopic data from X-Shooter at the Very Large Telescope (VLT) show that the lens is a typical early-type galaxy (ETG) at $z_l = 0.9906$, while the background source is a Lyα emitter at $z_s = 2.823$. The reference lens modeling was performed on a high-resolution *Y*-band adaptive-optics image from HAWK-I at VLT. Assuming a singular isothermal ellipsoid total mass density profile, we inferred an Einstein radius $R_{\rm Ein} = 10.47 \pm 0.06$ kpc. The average slope of the total mass density inside the Einstein radius, as determined by a joint analysis of lensing and isotropic Jeans equations, is $\gamma_{\rm tot} = 2.14^{+0.06}_{-0.07}$, showing no systematic deviation from the slopes of lower-redshift galaxies. This can be the evidence of ETGs developing through dry mergers plus moderate dissipationless accretion. Stellar population analysis with eight-band (*griZYJHK*$_s$) photometries from KiDS and VIKING shows that the total stellar mass of the lens is $M^* = (3.95 \pm 0.35) \times 10^{11}\ M_\odot$ (Salpeter initial mass function (IMF)), implying a dark matter fraction inside the effective radius of $f_{\rm DM} = 0.307 \pm 0.151$. We finally explored the dark matter halo slope and found a strong degeneracy with the dynamic stellar mass. Dark matter adiabatic contraction is needed to explain the posterior distribution of the slope, unless an IMF heavier than Salpeter is assumed.

Unified Astronomy Thesaurus concepts: Dark matter (353); Gravitational lensing (670); Galaxy dynamics (591); Galaxy formation (595); Galaxy evolution (594)

1. Introduction

Strong lensing is the effect of image distortion of faraway galaxies (sources) due to their light being bent by massive celestial bodies (lenses or deflectors), as predicted by general relativity. It is sensitive to the total mass, including dark matter (DM) and baryonic matter, and, as such, it is a crucial tool for studying the interplay between these two components (T. Treu & L. V. E. Koopmans 2004; L. V. E. Koopmans et al. 2006, 2009; T. Treu et al. 2006, 2011; M. W. Auger et al. 2009; A. S. Bolton et al. 2012; A. Sonnenfeld et al. 2013b, 2014; R. Li et al. 2018; Q. He et al. 2020; A. Etherington et al. 2023). With strong lensing, we can measure mass with very high precision, typically with 5% uncertainties (see, e.g., A. S. Bolton et al. 2008), whereas other methods, such as galaxy dynamics and X-rays, might face higher uncertainties (e.g., P. J. Humphrey & D. A. Buote 2006; N. R. Napolitano et al. 2010; C. Tortora et al. 2022; K. Zhu et al. 2023). More importantly, the latter techniques become less accurate as one goes to higher redshifts (see, e.g., S. Shetty & M. Cappellari 2014), where the strong-lensing method is more efficient instead (see, e.g., T. Treu & L. V. E. Koopmans 2004).

* Based on observations with OmegaCam@VST, VIRCAM@VISTA, HAWK-I, and XSHOOTER@VLT (Prog. ID: 107.22S8).

Strong lensing has been used as a probe of the ΛCDM predictions, as it offers insights into the assembly history of galaxies and their relationship with their DM halo centers (e.g., E. Fulton & J. E. Barnes 2001; W. Dehnen & D. E. McLaughlin 2005; S. Kazantzidis et al. 2006; C. Nipoti et al. 2009), or to probe the slope of the total mass (dark plus stellar mass) density. Statistical analyses of strong-lensing systems have consistently indicated that the total mass distribution of massive early-type galaxies (ETGs) follows a power-law profile, $\rho \propto r^{-\gamma}$, with $\gamma \approx 2$ and uncertainties below 10% (L. V. E. Koopmans et al. 2006, 2009; M. W. Auger et al. 2009; A. Sonnenfeld et al. 2013b; C. Tortora et al. 2014; C. Y. Tan et al. 2024), under the assumption of isotropic velocity dispersion. This result was further confirmed by dynamics, showing an isothermal (e.g., C. Tortora et al. 2016) or slightly steeper (e.g., $\gamma \sim 2.2$; S. Bellstedt et al. 2018; S. Li et al. 2024; K. Zhu et al. 2023, 2024; C. Wang et al. 2024) total mass density slope.

Hydrodynamical simulations have shown that $\gamma \sim 2$ is predicted at lower redshifts, where galaxy growth is driven by "dry" mergers (e.g., C. Nipoti et al. 2009; R.-S. Remus et al. 2017). However, the redshift evolution of γ is still debated, as simulations predict that the slope will become steeper ($\gamma > 2$) with increasing redshift (R.-S. Remus et al. 2017; Y. Wang et al. 2019), while some observations indicate a rather constant (A. Sonnenfeld et al. 2013b) or decreasing γ with redshift (A. S. Bolton et al. 2012; R. Li et al. 2018). Unfortunately, most of these measurements are limited to $z \lesssim 0.8$, with very few excursions to higher redshifts (MG 2016+112 at $z = 1.004$, CFRS 03.1077 at $z = 0.938$; L. V. E. Koopmans & T. Treu 2002; T. Treu & L. V. E. Koopmans 2002, 2004). Hence, this poor statistics of lenses at $z > 0.8$ is a serious handicap to resolving the controversy between observations and simulations.

Another major source of systematics in the mass slope problem is the assumed stellar initial mass function (IMF). This strongly impacts the stellar mass, M_*, and consequently the DM fraction $f_{\rm DM}$ of the foreground lens. Changes in the IMF normalization can increase the stellar mass-to-light ratio by more than a factor of 2, as evidenced by a large number of observations in massive elliptical galaxies (M. Cappellari et al. 2012; C. Conroy & P. G. van Dokkum 2012; F. La Barbera et al. 2013; C. Tortora et al. 2013; C. Spiniello et al. 2014; H. Li et al. 2017; S. Lu et al. 2024). The choice of the IMF significantly influences conclusions regarding the DM slope. Specifically, if the IMF leads to a higher estimate of stellar mass in the galaxy center, this implies that there is less DM present. Consequently, the DM density profile must be less steep to remain consistent with the observed stellar kinematics. On the other hand, for a lighter IMF, which leads to lower stellar mass M_*, steeper slopes have to be assumed to replace the missing stellar masses. This can be reconciled with ΛCDM only by invoking some form of adiabatic contraction (e.g., N. R. Napolitano et al. 2010; C. Tortora et al. 2010; T. Treu et al. 2010). The degeneracy between IMF assumptions and DM slope estimates becomes particularly problematic when considering the growing evidence that the IMF may not be universal (M. Cappellari et al. 2012; L. Greggio & A. Renzini 2012; C. Tortora et al. 2013; C. Spiniello et al. 2014; I. Martín-Navarro et al. 2015, 2024; C. E. Barbosa et al. 2021). Variations in IMF with galaxy mass, stellar population properties, and redshift introduce additional systematic uncertainties, as different galaxies may require distinct IMF prescriptions.

In our previous work (R. Li et al. 2021), we identified a blue Einstein ring candidate, KIDS J0233−3447, which was also independently discovered by G. Stein et al. (2022). Subsequent spectroscopic follow-up observations have confirmed that this object is a genuine strong lens with a foreground galaxy at redshift $z_l = 0.9906$. For the peculiar appearance in the optical bands, we have dubbed it the Einstein "blue eye" (see Figure 1). KIDS J0233−3447 is the second most distant lens for which such a detailed analysis (e.g., velocity dispersion, stellar mass, total mass density slope, DM fraction, and its density slope) has been performed (with MG 2016+112 mentioned above being the most distant one; L. V. E. Koopmans & T. Treu 2002) and among only a limited number of confirmed lenses at $z_l > 0.9$ (e.g., K. C. Wong et al. 2014; R. L. Barone-Nugent et al. 2015; R. Cañameras et al. 2017; L. Ciesla et al. 2020; P. van Dokkum et al. 2024), hence providing us a unique opportunity to move a step toward the understanding of the mass properties of galaxies in their early evolution phases.

In this paper, we present a comprehensive analysis of the stellar and DM properties of KIDS J0233−3447 and provide a detailed discussion of the IMF and the profiles of its total and DM mass. The paper is organized as follows: In Section 2, we introduce the data analysis. In Section 3, we provide a discussion of the results on the total mass slope, DM properties, and IMF model. Finally, in Section 4, we summarize our findings and draw our conclusions. For all calculations, we assume a ΛCDM cosmology with the WMAP7 (E. Komatsu et al. 2011) results: $(\Omega_\Lambda, \Omega_M, h) = (0.272, 0.728, 0.704)$.

2. Data Analysis and Key Parameters

In order to perform a complete, combined, and self-consistent lensing modeling, dynamics, and stellar population analysis on KIDS J0233−3447, we have collected seeing-matched *griZYJHK*$_s$ photometry from the Kilo-Degree Survey (KiDS; J. T. A. de Jong et al. 2013 A. H. Wright et al. 2024) and VISTA Kilo-degree Infrared Galaxy (VIKING; A. Edge et al. 2013) survey and a similarly wide wavelength baseline spectroscopy from X-Shooter, as well as the adaptive-optics (AO) near-IR (NIR) data from HAWK-I at the Very Large Telescope (VLT; see Section 2). Moreover, these data also offer the chance to assess the importance of optical + NIR data sets in strong-lensing analyses, for which the KiDS + VIKING data set is the only available precursor of optical + NIR joint analysis of Euclid (R. Laureijs et al. 2011), Vera C. Rubin Observatory (Ž. Ivezić et al. 2019), Roman (D. Spergel et al. 2015), and the China Space Station Telescope (H. Zhan 2011).

2.1. Spectroscopic Confirmation

KIDS J0233−3447 (R.A. = 02:33:41.29, decl. = −34:47:59.24) was discovered in the southern KiDS footprint through a machine learning search (R. Li et al. 2021). In that study, we trained a supervised convolutional neural network based on the ResNet (K. He et al. 2016) architecture, using simulated strong lenses as positive examples and real KiDS galaxies as negative examples. Applied to the full KiDS DR5 data set (∼350 deg^2), the classifier identified 97 high-quality lens candidates, of which KIDS J0233−3447 is particularly noteworthy. The *g*, *r*, *i* color image of this system shows two bright blue arcs that form an

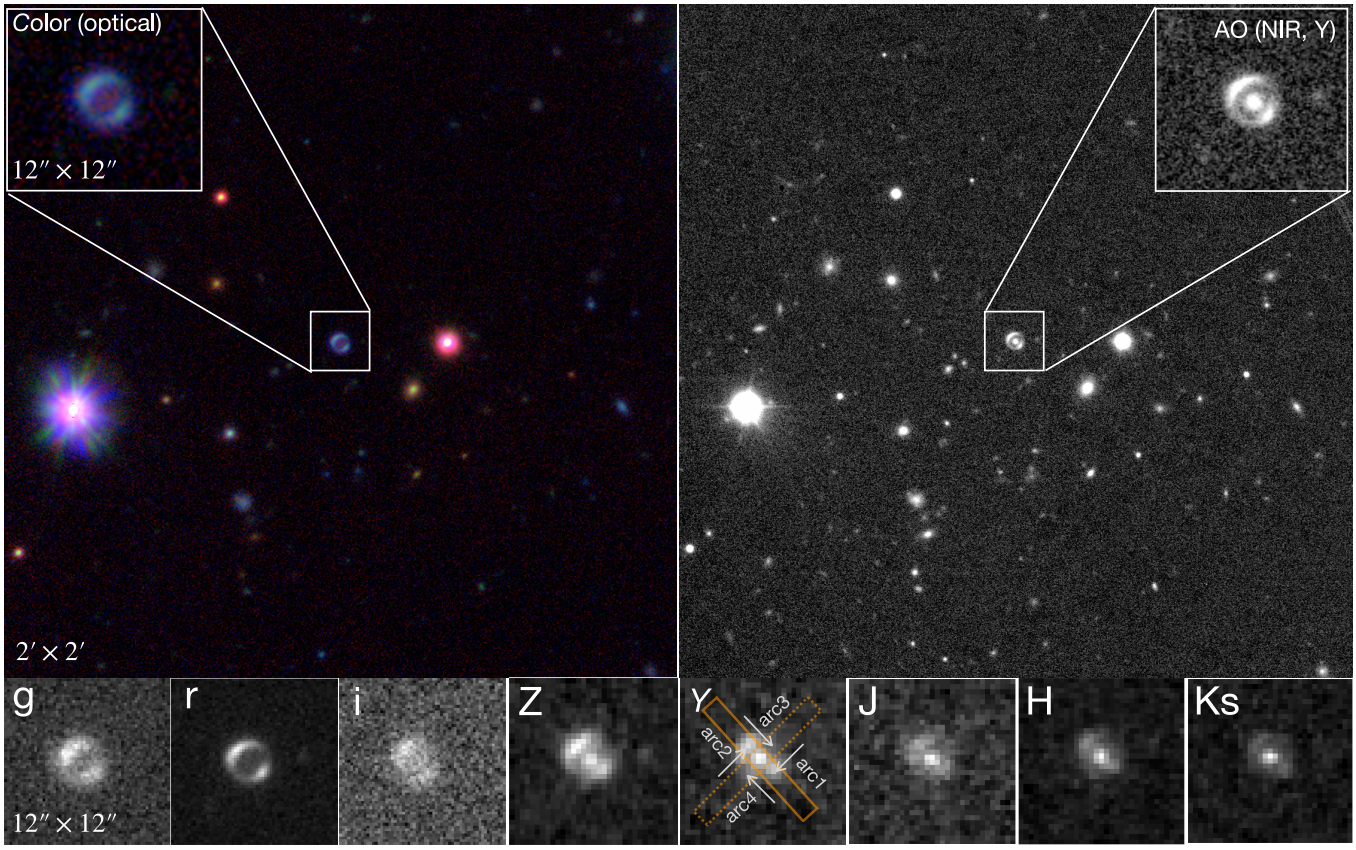

Figure 1. Images of KIDS J0233−3447. Top left: color-composite images (2′ × 2′) from KiDS observation and the zoom-in of the lens (12″ × 12″). Top right: *Y*-band image from HAWK-I@VLT (2′ × 2′) and the zoom-in of the lens (12″ × 12″). Bottom: eight-band images from KiDS and VIKING. The two slits used for the spectroscopical observations are shown in orange dashed (for lens) and solid (for arcs) rectangles on the *Y*-band image, respectively. White arrows labeled with arc1 to arc4 show the approximate location of the regions used to extract the spectra of the arcs (see Section 2.1).

almost perfect Einstein ring (see Figure 1). However, no central galaxy is visible in these optical observations. For the same system, the five-band NIR (*Z*, *Y*, *J*, *H*, K_s) images from the VIKING survey (A. Edge et al. 2013) show a small-sized galaxy in the center of the ring.

The optical−NIR spectroscopy was collected using the X-Shooter spectrograph at VLT (ID: 107.22S8; PI: Napolitano). The observations were made in the long-slit mode, with an average seeing of approximately 0.″9 and an air mass of ∼1.4. The length of the slits is 11″, and the widths for the lens are 1.″3, 1.″2, and 1.″2 in the UVB, VIS, and NIR arms, respectively, while those for the arcs are 1.″3, 1.″5, and 1.″5. The total integration time was 2.5 hr for the lens (three exposures of 3000 s each; orange dashed rectangle in Figure 1) and 1.25 hr for the arcs (two exposures of 2250 s each; orange solid rectangle). The two different slit orientations served to minimize the contamination of the arcs to the lens and vice versa.

Following the same method as in C. Spiniello et al. (2019), for the spectra observed in each slit and each arm, we decomposed the wavelength-calibrated, background-subtracted, and telluric-corrected 2D spectra into three components, two arcs, and a central galaxy, using the accurate astrometric information provided by the strong-lensing model performed on AO images (see Section 2.2). The VIS-arm spectrum of the central galaxy is shown in Figure 2. We fitted the spectrum of the central galaxy with PPXF (M. Cappellari 2017) and found it to follow an elliptical galaxy template at $z_l = 0.9906 \pm 0.0001$, showing evident features of absorption lines of [*K*], [*H*], and *G* band. We have estimated a stellar velocity dispersion inside the slit (VIS, 1.″2 width, orange slit in Figure 1) of 309 ± 35 km s^{-1}, using the region surrounding the prominent [*K*] and [*H*] lines. The fitting also shows a double-peak star formation history (SFH) at the ages of ∼3 and ∼6 Gyr (see the lower right corner in the first row). We confirmed the lensing nature of the images by comparing the four spectra decomposed in the two slits (arc1, arc2, arc3, and arc4; see, in particular, the UVB in Figure 2), as they show a very similar continuum with the same absorption/emission lines (e.g., Lyα, C[III], [O II], and O[III] emissions). Finally, we determined the source redshift from these lines in the mean spectrum of the four components, and it is $z_s = 2.823 \pm 0.001$.

2.2. Lensing Model with AO Image

The *Y*-band AO images were obtained with HAWK-I@VLT under the same ESO program and were reduced by the HAWK-I Pipeline.[21] The final processed stacked image has a pixel scale of 0.″1065 pixel^{-1} and a point-spread function (PSF) of 0.″46 (full width at half-maximum (FWHM)), with a deeper exposure than those from KiDS and VIKING, making it ideal for accurate lensing modeling.

[21] https://www.eso.org/sci/facilities/paranal/instruments/hawki/doc.html

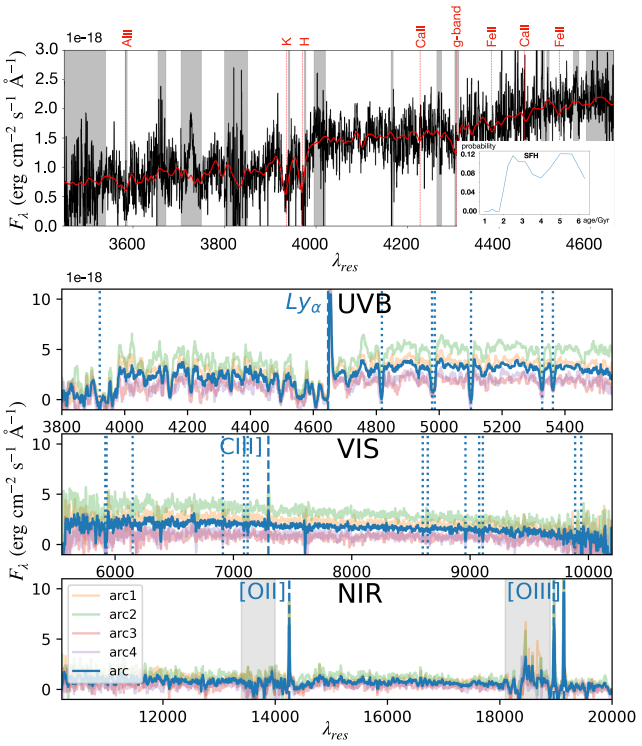

Figure 2. Top: optical arm of the spectra of the deflector (in rest frame), obtained from X-Shooter. The 4000 Å break can be seen. The velocity dispersion can be inferred from the two characteristic absorption lines, e.g., [*K*] and [*H*] bands, of elliptical galaxies. Bottom: the spectra of the lensed source in the NUV, VIS, and NIR arms. The four arcs are decomposed from the two slits of different orientations (see Figure 1). The blue line shows the average flux of the four arcs. The Lyα, O II, and O III lines demonstrate that the background source is a Lyα emitter at $z_s = 2.823$.

The modeling was performed using the LENSED code (N. Tessore et al. 2016), which allows for simultaneous modeling of the mass and light distributions. For the light distribution of the lens galaxy, we tested both a de Vaucouleurs profile (G. de Vaucouleurs 1948) and a more flexible Sérsic profile (J. L. Sérsic 1963). Both profiles provide an excellent fit to the lens galaxy's light. However, the choice significantly impacts the derived effective radius (R_e). We found that the Sérsic model yields a considerably larger effective radius compared to the de Vaucouleurs model (see Table 1). This leads to a much higher estimate for the DM fraction within R_e in our following analysis, as this fraction is sensitive to the radius of measurement. A primary goal of this work is to directly compare the scaling relations of KiDS J0233−3447 with SLACS (A. S. Bolton et al. 2008) and SL2S (A. Sonnenfeld et al. 2013b) lens samples, as well as with simulations (C. Nipoti et al. 2009), which predominantly used the de Vaucouleurs profile for consistency. Using Sérsic-derived parameters would introduce a systematic bias. Therefore, to ensure a robust comparison, we adopt the de Vaucouleurs profile as our fiducial choice for the main analysis. For full transparency, we report the key results from both light models in our analysis on the AO image (see Table 1). Since the source is a Lyα emitter and very little is known about the structure of these galaxies, we decided to use a Sérsic profile for the light distribution. Finally, we modeled the total mass distribution of the deflector using a singular isothermal ellipsoid (SIE; R. Kormann et al. 1994) profile. The SIE model was selected for its ability to accurately recover the

Table 1
Summary of the Key Parameters of the Lens System

Parameters	de Vaucouleurs	Sérsic
X-Shooter Spectroscopy		
z_l	0.9906 ± 0.0001	0.9906 ± 0.0001
z_s	2.8230 ± 0.0001	2.8230 ± 0.0001
$\sigma_{\rm slit}$ (km s^{-1})	309 ± 35	309 ± 35
$\sigma_{\rm Re}$ (km s^{-1})	343 ± 37	335 ± 37
Lensing Model (Based on AO Image)		
$R_{\rm Ein}$ (arcsec)	1.2926 ± 0.008	1.2899 ± 0.006
$R_{\rm Ein}$ (kpc)	10.47 ± 0.06	10.45 ± 0.05
Lens mass b/a	0.932 ± 0.008	0.933 ± 0.007
Lens mass PA	141.1 ± 3.8	141.0 ± 3.9
Lens light n-index	4.0 (fixed)	5.60 ± 0.78
Lens light b/a	0.85 ± 0.08	0.85 ± 0.08
Lens light PA	122.6 ± 59.8	117.8 ± 58.8
Lens light $R_{\rm eff}$ (arcsec)	0.4392 ± 0.057	0.6206 ± 0.1252
Lens light $R_{\rm eff}$ (kpc)	3.56 ± 0.46	5.03 ± 1.01
Source n-index	1.42 ± 0.26	1.34 ± 0.27
Source b/a	0.76 ± 0.09	0.83 ± 0.09
Source $R_{\rm eff}$ (arcsec)	0.123 ± 0.017	0.124 ± 0.023
Source $R_{\rm eff}$ (kpc)	0.986 ± 0.136	0.991 ± 0.184
Dynamic and Mass Estimates		
$\gamma_{\rm tot}$	$2.195^{+0.086}_{-0.097}$	$2.202^{+0.093}_{-0.106}$
$M_{\rm Ein}/(10^{11}\,M_\odot)$	7.183 ± 0.067	7.213 ± 0.089
$M_{\rm tot}^{\rm eff}/(10^{11}\,M_\odot)$	2.848 ± 0.369	3.805 ± 0.717
$M_*/(10^{11}\,M_\odot)$ (Chab)	2.31 ± 0.20	2.06 ± 0.23
$M_*/(10^{11}\,M_\odot)$ (Salp)	3.95 ± 0.35	3.71 ± 0.38
$f_{\rm DM}(R_{\rm eff})$ (Chab)	0.594 ± 0.088	0.729 ± 0.081
$f_{\rm DM}(R_{\rm eff})$ (Salp)	0.307 ± 0.151	0.512 ± 0.141

Note. The key parameters of the lens system. The first line specifies the lens light in the modeling. X-Shooter spectroscopy: redshift of the lens (z_l) and source (z_s), and the velocity dispersion of the lens calculated in the slit and at $R_{\rm eff}$. Lensing models from the AO image: Einstein radius ($R_{\rm Ein}$) in arcsec and kpc, followed by self-explaining parameters related to the total mass (labeled by "lens mass"), lens light profile (labeled by "lens light"), and source light profile (labeled by "source"). Dynamic and mass estimates: summary of the total mass density slope (γ), mass estimates from the lensing model ($M_{\rm Ein}$), and stellar population $M_*^{\rm SED}$ (see text for details), together with the projected DM fractions ($f_{\rm DM}$).

total mass enclosed within the Einstein radius. This total mass measurement is subsequently employed in the combined lensing and dynamical analysis to derive the total mass density slope (see Section 2.3). In the model process, the centers of the mass and light distributions were treated as independent parameters. The best-fit results show that they are coincident to within $0\farcs06$, which is only slightly larger than half a pixel in the AO imaging. We also tested for the presence of an external shear component but found it to be negligible ($\gamma_{\rm shear} < 0.02$), and its inclusion did not impact our final results. We therefore did not include it in our final model.

In the first row of Figure 3, we show the *Y*-band AO image, the best-fitting model, and the residuals obtained by LENSED. The main parameters obtained from the lens modeling are listed in Table 1. The Einstein radius is $R_{\rm Ein} = 10.47 \pm 0.06$ kpc, corresponding to an Einstein mass of $M_{\rm Ein} = (7.213 \pm 0.089) \times 10^{11}\,M_\odot$. The axis ratio for the total lensing mass is 0.932 ± 0.008, which is a little rounder than the axis ratio of the light, $b/a = 0.85 \pm 0.08$, but consistent

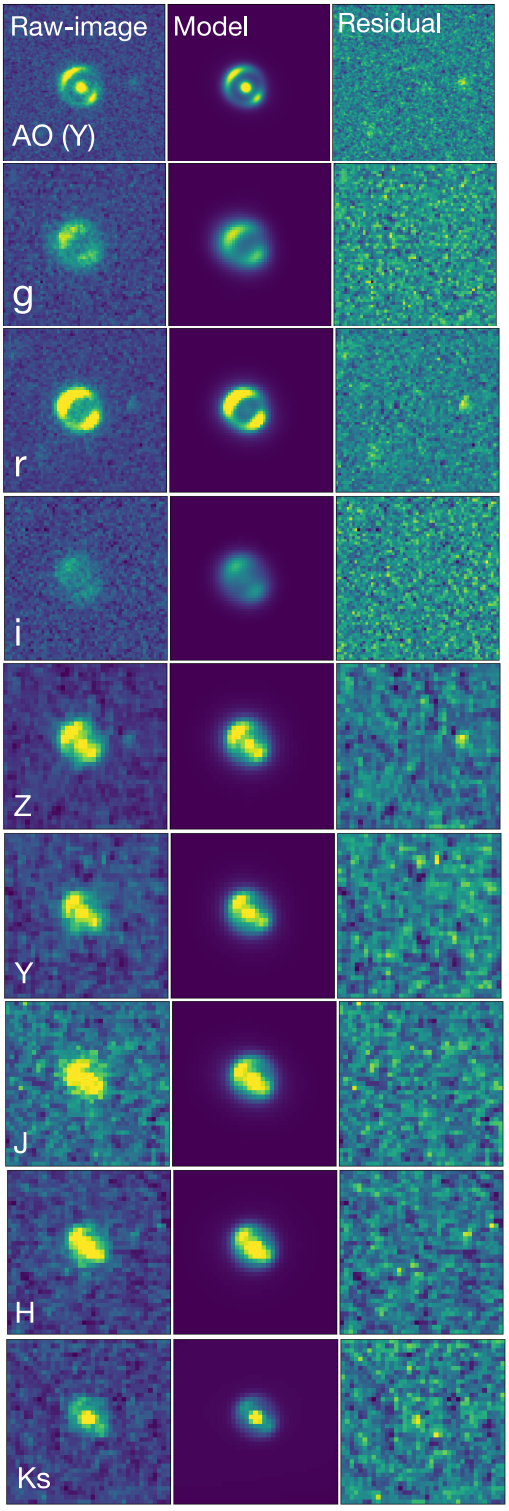

Figure 3. Multiband strong-lensing model of KIDS J0233−3447. From top to bottom, we show the modeling of the AO (*Y*-band) image, three optical (*g*, *r*, *i*) images, and five NIR (*Z*, *Y*, *J*, *H*, K_s) images. In each band, the left, middle, and right panels show the observed data, the lens model, and the residuals, respectively.

with the latter within the 1σ error. The effective radius of the deflector is $R_{\rm eff} = 3.56 \pm 0.46$ kpc, about $1/3$ of $R_{\rm Ein}$. These properties imply that the deflector is a massive elliptical galaxy with a round shape. The effective radius and the Sérsic index n of the source are $R_{\rm eff} = 0.991 \pm 0.184$ kpc and $n = 1.34 \pm 0.27$, respectively, which are typical values for Lyα emitters at $z \sim 3$ (e.g., Y. Shu et al. 2016a, 2016b).

In order to check the robustness of the lens modeling, we have conducted an additional round of modeling and its subsequent analysis (including Sections 2.3 and 2.4), employing a Sérsic profile for the central foreground galaxy. The parameters obtained from this analysis are also listed in Table 1. Upon comparison, it is observed that the parameters derived from the assumption of a Sérsic central galaxy are in concordance with those obtained from the de Vaucouleurs model, with the exception of the effective radius $R_{\rm eff}$. This discrepancy in $R_{\rm eff}$ subsequently influences the estimation of the total mass and the fraction of DM enclosed within the effective radius. Within the scope of this study, we will concentrate on the de Vaucouleurs model for our foreground central galaxy assumption. Consequently, we will not delve into an in-depth discussion of the outcomes associated with the Sérsic central galaxy hypothesis.

2.3. Joint Lensing and Dynamical Analysis

By combining the ray-tracing lens modeling and the dynamics of the central galaxy, we have enough constraints to infer more detailed properties of the total mass of the lensing system, e.g., its central slope (see, e.g., T. Treu & L. V. E. Koopmans 2002). For this purpose, we have assumed that the density distribution of the lens galaxy in three dimensions follows a power-law profile of the form

$$\rho = \rho_0 \left(\frac{r}{r_0}\right)^{-\gamma}, \tag{1}$$

where ρ_0 and r_0, jointly, can be determined by the Einstein mass and Einstein radius, and γ denotes the logarithmic slope. We then solve the spherical Jeans equation (J. Binney & S. Tremaine 1987)

$$\frac{1}{\nu}\frac{d(\nu\overline{v_r^2})}{dr} + 2\frac{\beta\overline{v_r^2}}{r} = -\frac{GM(<r)}{r^2}, \tag{2}$$

where ν represents the density of the light particles in the galaxy, assumed to be proportional to the three-dimensional light distribution. The anisotropy parameter, β (L. P. Osipkov 1979; D. Merritt 1985), is set to be 0 (isotropic orbits) in our analysis, consistent with many works that analyze the velocity dispersion of massive ETGs (e.g., M. W. Auger et al. 2009; L. V. E. Koopmans et al. 2009). Finally, $M(<r)$ denotes the total mass contained within a sphere of radius r, corresponding to the density in Equation (1). We performed the lensing and dynamical analyses following the method described in R. Li et al. (2018; see also L. V. E. Koopmans et al. 2006, 2009; A. S. Bolton et al. 2012; A. Sonnenfeld et al. 2013b). Briefly, the method consists of minimizing the χ^2 between the velocity dispersion obtained by projecting the solution of Equation (2) within an aperture corresponding to the effective radius and the observed one within the same aperture. At each iteration of the χ^2, the $M_{\rm Ein}$ and $R_{\rm Ein}$ are used to derive the ρ_0 in Equation (1) used to solve Equation (2). The atmospheric seeing and the aperture luminosity weighting function are also considered (see details in J. Schwab et al. 2010). We found the best-fit total mass density slope to be $\gamma_{\rm tot} = 2.14^{+0.06}_{-0.07}$. Assuming a power-law mass distribution, the total mass

within the $R_{\rm eff}$ (consisting of both stellar and DM) was determined to be $M_{\rm tot}^{\rm eff} = (2.85 \pm 0.37) \times 10^{11}\,M_{\odot}$.

2.4. Stellar Population from Eight-band Ray-tracing Model

We took advantage of the optical plus NIR photometry from KiDS and VIKING to derive the stellar population parameters of the lens, given that the signal-to-noise ratio of the X-Shooter spectra is insufficient to perform a detailed study of the spectral indices. We have performed the lensing model on eight-band (*griZYJHK*$_s$) images to derive accurate and uncontaminated multiband magnitudes for the central galaxy. The light of the central galaxy is fitted with a de Vaucouleurs profile, while the mass is assumed to be SIE. Details about the modeling can be found in the Appendix. We show the model and residuals in Figure 3 for a sample of KiDS and VIKING bands, including the *Y* band to confront the AO model.

We performed the spectral energy distribution (SED) fitting with the multiband photometry using the CIGALE code. For this analysis we have assumed G. Bruzual & S. Charlot (2003, hereafter BC03) stellar population templates. Parameters, such as the metallicity, extinction, star-forming rate, and age of the main stellar population, were set free to vary. We used both a Chabrier IMF and a Salpeter IMF, which returned a total stellar mass of $M_{\rm SED}^{\rm Chab} = (2.31 \pm 0.20) \times 10^{11}\,M_{\odot}$ and $M_{\rm SED}^{\rm Salp} = (3.95 \pm 0.35) \times 10^{11}\,M_{\odot}$, respectively. Given $R_{\rm eff} = 3.56 \pm 0.46$ kpc, we found that the mass–size relation of this galaxy is fully consistent with ETGs at redshift $z \sim 1$ (see A. Sonnenfeld et al. 2013b). Finally, by subtracting the stellar mass from the total mass, we obtained the DM mass and then the DM fraction inside the effective radius, which are $f_{\rm DM}^{\rm Chab} = 0.594 \pm 0.088$ for the Chabrier IMF and $f_{\rm DM}^{\rm Salp} = 0.307 \pm 0.151$ for the Salpeter IMF.

The stellar population analysis returned a galaxy age of 5.9 (Chabrier IMF) or 5.6 Gyr (Salpeter IMF), suggesting an old stellar population and an early formation epoch but with a rather extended delayed SFH $\propto t/\tau^2 \exp(-t/\tau)$, with a $\tau \sim 0.8$ Gyr. The old age has been confirmed by the PPXF analysis of the X-Shooter spectra showing a double-peaked SFH, at $\sim$5.5 and $\sim$2.5 Gyr in look-back time (see the top panel of Figure 2), hence fully compatible with old age and an extended SFH. This is a much older age than the one found from another high-z lens, MG 2016+112, which shows younger stellar populations (T. Treu & L. V. E. Koopmans 2002).

3. Discussion on the Properties

3.1. Total Mass Density Slope and Dark Matter Fraction

As mentioned above, the lensing galaxy KiDS J0233−3447 is the second galaxy at $z_l \sim 1$ for which a total density slope measurement has been obtained after MG 2016+112. The latter system has many similarities with KiDS J0233−3447, such as the lens and source redshift and the velocity dispersion inside the effective radius. The exact values are listed below:

1. *KiDS J0233−3447*: $z_l = 0.9906$, $z_s = 2.823$, $\sigma_{R_e} = 343 \pm 37$ km s^{-1}, and $\gamma_{\rm tot} = 2.14^{+0.06}_{-0.07}$.
2. *MG 2016+112*: $z_l = 1.004$, $z_s = 3.263$, $\sigma_{R_e} = 304 \pm 27$ km s^{-1}, and $\gamma_{\rm tot} = 2.0 \pm 0.1$.

While the total density slopes, $\gamma_{\rm tot}$, are consistent with each other within their 1σ uncertainties, the value for KiDS J0233−3447 is notably steeper and deviates from a purely isothermal profile ($\gamma_{\rm tot} = 2$) at the 2σ level. In contrast, the slope of MG 2016+112 is perfectly consistent with an isothermal distribution. This difference in $\gamma_{\rm tot}$ likely reflects the distinct evolutionary histories of the two galaxies. The steeper slope in KiDS J0233−3447 suggests a more significant baryonic concentration at its center, which in turn induces a stronger adiabatic contraction of the DM halo compared to MG 2016+112. We present a detailed analysis of this scenario, which connects the stellar IMF to the halo contraction, in Section 3.2.

A. J. Ruff et al. (2011) and A. S. Bolton et al. (2012) claimed that the total mass density slope $\gamma_{\rm tot}$ should increase with cosmic time. However, this appears inconsistent with simulations of dry merger-driven evolution in ETGs. C. Nipoti et al. (2009) suggested that dry mergers might preserve the nearly isothermal structure of galaxies during $0 < z < 1$. Later analyses by A. Sonnenfeld et al. (2014) demonstrate that pure dry mergers predict a substantial decrease in density slope over time, conflicting with lensing observations indicating either increasing or constant $\gamma_{\rm tot}$. When incorporating modest dissipative processes (e.g., gas accretion), the central density profile can steepen, offsetting the flattening effects of dry mergers. This mechanism enables $\gamma_{\rm tot}$ to remain constant from $z \sim 1$ to $z = 0$.

Given the scarcity of gas in ETGs to allow wet mergers, the only viable reconciliation between observations and simulations requires nonevolution of $\gamma_{\rm tot}$ with redshift. SL2S lenses ($0 \lessapprox z \lessapprox 0.8$) measured $\gamma_{\rm tot} = 2.05 \pm 0.06$ (A. Sonnenfeld et al. 2013b). While SLACS samples previously suggested slightly steeper slopes ($\gamma_{\rm tot} = 2.078 \pm 0.027$), recent work by A. Sonnenfeld (2024) reveals that these measurements may be overestimated by $\sim$0.1 owing to selection biases. Lenses at $z \sim 1$ like KiDS 0233−3447 and MG 2016+112 exhibit slopes comparable to these lower-redshift lenses. We therefore suggest that the "blue eye" shows no systematic deviation from low-redshift slopes, supporting slope stability at $z < 1$ (e.g., L. V. E. Koopmans et al. 2006; A. Sonnenfeld et al. 2013b). This evidence suggests ETG evolution through combined dry mergers and moderate dissipationless accretion. Such hybrid evolution simultaneously explains observed size growth and $\gamma_{\rm tot}$ stability.

However, the total density slope $\gamma_{\rm tot}$ is a combination of (1) the shallower (typically $\sim$1) DM and the steeper (typically $\sim$3) stellar matter slopes (see, e.g., A. W. Graham et al. 2006) in the galaxy centers and (2) their relative mass fraction. A larger DM fraction generally leads to a shallower total density profile, closer to the DM slope, while a lower DM fraction would produce a slope more biased toward the steeper starlight. Interestingly, when DM and stars almost balance, the slope conspires toward an isothermal value, $\gamma_{\rm tot} \sim 2$. Lens systems indeed show a variety of slopes and a correlation with $f_{\rm DM}$ that follows this intuitive picture, as can be seen in the left panel of Figure 4. Here we show the correlation between the density slope $\gamma_{\rm tot}$ and the DM fraction $f_{\rm DM}^{\rm Salp}$ for the SL2S sample from A. Sonnenfeld et al. (2013b). We have chosen the SL2S sample for uniformity on the model assumptions, as they provide the $f_{\rm DM}$ inside the effective radius $R_{\rm eff}$, like us, and unlike SLACS (M. W. Auger et al. 2009), using half $R_{\rm eff}$. In addition, SL2S employs multiband photometry to calculate the stellar mass, although they have a narrower wavelength baseline than ours. Finally, the SL2S sample covers a wider redshift range than the SLACS, with the highest-z lens at

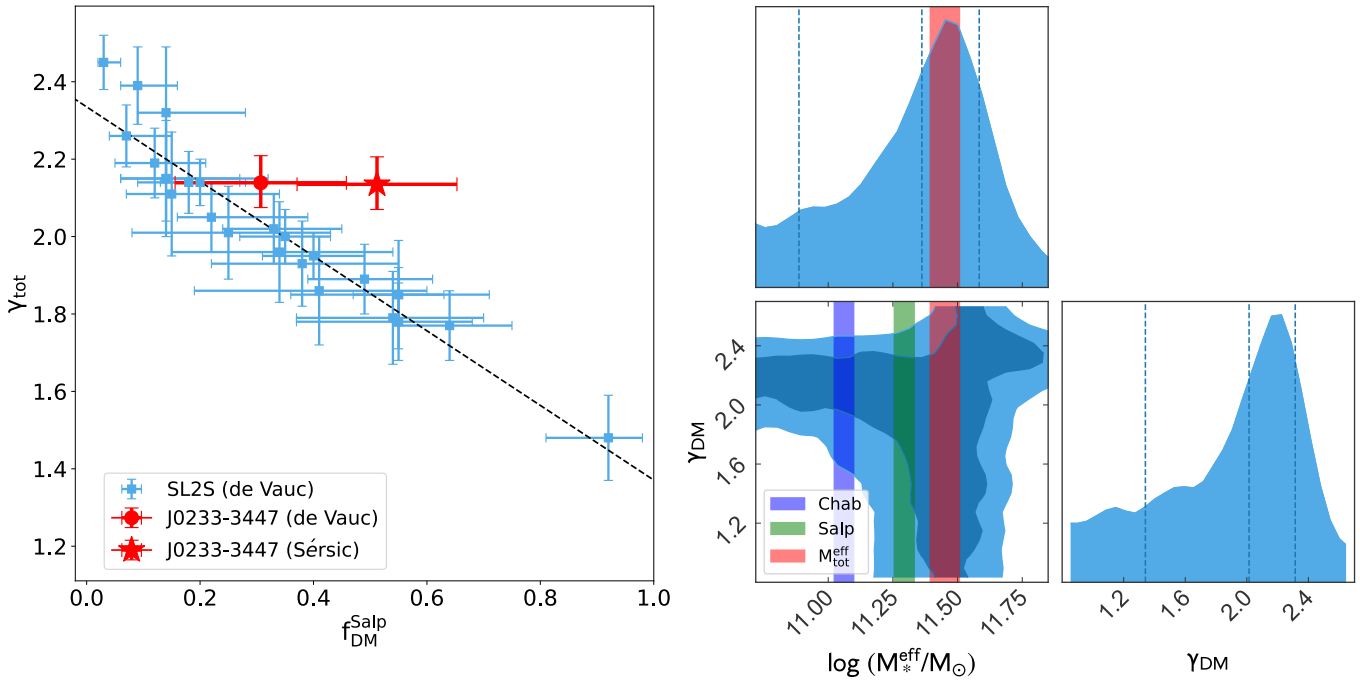

Figure 4. Left: the relationship between total mass density slope γ_{tot} and DM fraction (Salpeter IMF, f_{DM}^{Salp}) for the SL2S sample (squares) and of KiDS J0233−3447 by assuming a de Vaucouleurs (circle) and Sérsic (star) foreground light profile. The black dashed line shows the line fit of the SL2S sample. Right: the MCMC inference for DM slope γ_{DM} and the stellar mass inside the R_{eff}. The stellar masses inferred from the Chabrier and Salpeter IMFs (also inside the R_{eff}) are shown with blue and green bars, respectively.

$z \sim 0.781$, closer to the redshift of the Einstein "blue eye." Finally, we use the de Vaucouleurs profile as in SL2S.

In Figure 4, KiDS J0233−3447 shows a $\gamma_{tot} = 2.14^{+0.06}_{-0.07}$, which is fully consistent with the correlation from the SL2S sample. In the same figure, we also show that the situation is different if we assume a Sérsic model for the foreground galaxy instead of a de Vaucouleurs one (full lensing parameters reported in Table 1), mainly due to the larger R_{eff}. We might expect that a similar correction toward larger DM fraction could apply to the SL2S sample if a Sérsic model were adopted, but, overall, the conclusion about the consistent trend between f_{DM} and γ would remain unchanged, not certainly worsened.

Here we note that the observed γ_{tot}–f_{DM} relation in the SL2S sample, as well as in other lensing samples (e.g., SLACS; A. J. Shajib et al. 2021), exhibits discrepancies with cosmological simulations. Hydrodynamical simulations either reproduce the γ_{tot} distribution but systematically underestimate f_{DM} when baryonic physics is minimally included (e.g., A. R. Duffy et al. 2010; P. H. Johansson et al. 2012) or recover the observed f_{DM} with strong feedback at the expense of predicting shallower slopes than observed (e.g., Y. Dubois et al. 2013; D. Xu et al. 2017). The γ_{tot}–f_{DM} relation of KIDS J0233−3447 aligns with previous lensing studies at lower redshifts (e.g., A. Sonnenfeld et al. 2013a; A. J. Shajib et al. 2021), indicating that the tension with simulations also exists at higher redshift ($z \sim 1$). This persistent mismatch highlights the need for either refined implementations of feedback mechanisms in cosmological simulations or a critical reexamination of potential systematic biases in observational analyses.

3.2. IMF and Dark Matter Slope

The analysis presented in Section 3.1 adopts the Salpeter IMF as a wavelength baseline for comparison, aligning with the approach utilized in the SL2S study. It is acknowledged, however, that the IMF is not necessarily confined to the Salpeter IMF, with evidence suggesting variations in the IMF across different galaxies. The choice of IMF influences the estimation of the DM fraction, which, in turn, has implications for the measurement of the DM density slope. Specifically, the possibility that KiDS J0233−3447 favors a lighter or a heavier IMF, for a fixed total slope, has direct consequences for the inferred DM halo density slope. For instance, a higher DM fraction given from a lighter IMF would imply an excess of DM that might not be compatible with some standard ΛCDM halo. Hence, we need to evaluate how much the DM slope can vary in response to some physically motivated IMF variation.

To check this, we have combined lensing and dynamics again. But instead of a single power law, we consider the total mass of the galaxy in Equation (2) made of the stellar and DM components and then use Bayesian inference to obtain the posterior distribution of dynamical stellar mass and DM slope. The stellar mass is assumed to follow the de Vaucouleurs profile, as in Table 1, with a dynamical mass-to-light ratio as a free parameter ($M_*^{dyn}(r) = M/L_*^{dyn} \times L_{tot}^{deV}(r)$, with $L_{tot}^{deV}(r)$ being the growth curve of the deprojected de Vaucouleurs profile). Here we continue to employ the de Vaucouleurs profile to ensure a robust and direct comparison with key findings in the literature (e.g., C. Nipoti et al. 2009; A. Sonnenfeld et al. 2013b), as has been demonstrated in Section 2.2. Adopting a Sérsic profile would systematically alter the derived DM fraction, biasing any such comparison and thus affecting our conclusions. For the DM component, we adopt a power-law density profile, $\rho_{DM}(r) \propto r^{-\gamma_{DM}}$ (e.g., A. A. Dutton & T. Treu 2014; A. Sonnenfeld et al. 2015). This allows for a direct comparison with the standard Navarro–Frenk–White (NFW) profile, which features an inner slope of $\gamma_{DM} = 1$ and provides a good description of DM halos in

cosmological
N-body simulations (J. F. Navarro et al. 1997). To probe how the slope might change with a physically motivated IMF variation, we treat $\gamma_{\rm DM}$ as a free parameter in our Bayesian inference. Finally, we note that the stellar mass obtained here is dynamically inferred and we can use its ratio with the SED/IMF inferred stellar masses, as a proxy of the variation of the IMF.

In Figure 4, we report the confidence contours (68% and 95%) and the marginalized posterior probabilities (16%, 50%, and 84%, vertical dashed lines from left to right) of the two parameters in our model. To have a more physical insight of the inferences, on the x-axis we report the stellar mass inside the $R_{\rm eff}$ corresponding to the inferred $M/L_*^{\rm dyn}$, as this can be compared with the inferences of the SED/IMFs (namely the Chabrier and Salpeter IMFs) and with the total mass inside the same radius from the lensing and dynamics, all marked as vertical stripes in the figure. The latter value provides a physical upper limit for the stellar mass, as the mass in stars cannot exceed the total enclosed mass. It is plotted for a posteriori comparison and helps to interpret the physical region of the parameter space.

From the confidence contours, we see a degeneracy between $M_*^{\rm eff}$ and $\gamma_{\rm DM}$. IMF normalizations above a Salpeter IMF are compatible with a larger variety of DM slope, between $\gamma_{\rm DM}\sim 2.3$ and down to $\gamma_{\rm DM}\sim 1$. However, using the $M_{\rm tot}^{\rm eff}$ as a physical upper limit for the stellar mass, we see that the accessible parameter space at low $\gamma_{\rm DM}$ is strongly restricted. A reasonable solution for an IMF steeper than the Salpeter IMF should have a stellar mass $\log M_*^{\rm eff}=11.36\pm0.05$ (i.e., around the lower limit of $M_{\rm tot}^{\rm eff}$) and a $\gamma_{\rm DM}\sim 1.6\pm0.6$, which would correspond to an $f_{\rm DM}=0.20$, perfectly reconciling the "blue eye" with the SL2S sample (see Section 3.1). This case is statistically consistent with a standard NFW profile, because the NFW inner slope of $\gamma_{\rm DM}=1$ lies within the 1σ confidence interval of our measurement, which is $\gamma_{\rm DM}\sim 1.6\pm0.6$.

On the other hand, if one wants to stick to a Salpeter IMF, $\log M_*^{\rm eff}=11.30\pm0.04$ and $\gamma_{\rm DM}\sim 2.0\pm0.4$, which would correspond to an $f_{\rm DM}=0.31$ (see also the lensing and dynamics analysis presented in Section 3.1). Considering that the DM slope is estimated within the $R_{\rm eff}$, we can follow N. R. Napolitano et al. (2010; see also A. W. Graham et al. 2006) and assume a dilution of the DM slope of $\Delta\gamma_{\rm DM}\sim 0.3$ with respect to the true central cusp, to find that this case is clearly steeper than an NFW profile ($\gamma_{\rm DM}^{\rm true}=2.0-0.4>1.0\pm0.3$) and more compatible with a contracted halo. A similar conclusion was also reached by A. Sonnenfeld et al. (2012), who analyzed a double Einstein ring lens at a low redshift ($z=0.222$) and inferred a DM slope of $\gamma_{\rm DM}=1.7\pm0.2$, and N. R. Napolitano et al. (2010), who found $\gamma_{\rm DM}\sim 1.6$ for a sample of local galaxies. Such a coexistence of Salpeter IMF and DM halo contraction has also been found in other works (e.g., C. Tortora et al. 2010; T. Treu et al. 2010; C. Spiniello et al. 2011; A. Sonnenfeld et al. 2013b), suggesting that it can be a regular feature in massive elliptical systems (but see J. T. Mendel et al. 2020).

Finally, according to the posterior probability, we cannot rule out the possibility of a lighter IMF than the Salpeter IMF, which would still require a steep DM slope, and thus imply a contracted halo. In particular, we see that a Chabrier or even lighter IMF is compatible with a steep DM slope up to $\gamma_{\rm DM}\gtrsim 2.0$, which is strongly deviating from the ΛCDM DM-only simulation predictions (i.e., an NFW profile; J. F. Navarro et al. 1997). The main implication of such an IMF would be an increased DM fraction of $f_{\rm DM}\sim 0.6$ (see Table 1). Such a DM fraction is larger than typical values found in observations for lower-redshift galaxies (e.g., COMA, J. Thomas et al. 2007; SLACS, $f_{\rm DM}<0.6$, M. Barnabè et al. 2011) and almost twice that expected from simulations for a Chabrier IMF at $z\sim 1$ (L. Oser et al. 2010; R.-S. Remus et al. 2017).

Although the arguments discussed above support both the Salpeter and Chabrier IMFs with a contracted halo, we can provide more direct evidence to support that KiDS J0233−3447 favors a heavier IMF (e.g., Salpeter) combined with contraction over a standard uncontracted NFW profile. Indeed, in a heavy halo contraction, one expects the dissipation of cold gas to play a strong role (see, e.g., O. Y. Gnedin et al. 2004; J. A. Sellwood & S. S. McGaugh 2005). According to the inferred SFH, from both the multiband photometry and the X-Shooter spectrum, the "blue eye" central galaxy has gone through a quite long and massive star formation activity, which lasted for ∼6 Gyr and ended just before $z\sim 1$. In particular, the double-peaked SFH suggested by PPXF might even suggest a major accretion event. We argue that this extended SFH might have favored the halo contraction of the central galaxy. We remark here that an extended (even double-peaked) SFH is consistent with the two-stage formation model proposed by C. Weidner et al. (2013) that can explain both a bottom-heavy IMF and a solar metallicity observed in high-z ETGs. According to this model, galaxies have formed ∼10% of their stars during a very short burst, lasting 0.3 Gyr, with a top-heavy IMF, followed by a second stage where the bulk of the stellar mass is formed in about 1 Gyr, with a bottom-heavy IMF. If so, the "blue eye" central galaxy can be a test bench of this model, showing eventually even a more prolonged process, possibly driven by the higher velocity dispersion (and hence mass) of KIDS J0233−3447, with respect to the typical galaxies considered in C. Weidner et al. (2013).

4. Conclusion

We have provided the first full optical + NIR photometric and spectroscopic analysis of an Einstein ring at $z\sim 1$. KiDS J0233−3447 is a strong lens candidate discovered in KiDS in R. Li et al. (2021), which we followed up with the X-Shooter and HAWK-I instruments at VLT. The foreground galaxy is an ETG located at $z_l=0.9906$, while the background source is a Lyα emitter at $z_s=2.832$.

We collected a combined multiband (optical to infrared), AO, and spectroscopic data set for this lens, which allowed us to perform a complete multiband analysis of the system, including an eight-band lens model. With the analysis, we can constrain the lens parameters in the eight-band models with excellent accuracy, despite the different seeing conditions and image quality of the cameras adopted. The Einstein radius and effective radius are 10.47 ± 0.06 kpc and 3.56 ± 0.46 kpc, respectively, and the total mass density slope (obtained via lensing-dynamical analysis) is $2.139^{+0.064}_{-0.070}$, which is close to the isothermal density profile, consistent with previous lower-redshift strong lenses. This supports a scenario of dry merger plus modest dissipative processes (such as gas accretion) driving the ETG evolution between $0<z<1$ (A. Sonnenfeld et al. 2014).

We reported a DM fraction within $R_{\rm eff}$ to be $f_{\rm DM}=0.307\pm0.151$ (assuming a Salpeter IMF), which is consistent with values typically observed in strong-lensing systems at lower redshifts and similar masses. To explore

whether this DM fraction could result from an unaccounted heavier IMF, we found that such a scenario would imply a standard NFW halo (i.e., $\gamma_{\rm DM=1}$) with $f_{\rm DM} \sim 0.20$. On the other hand, if we assume a Salpeter IMF, the observed DM fraction would suggest a contracted halo with a DM slope of $\gamma_{\rm DM} > 1.6$, consistent with other evidence from low-redshift galaxies.

The old age ($\sim$6 Gyr) and the extended SFH, derived by both the eight-band photometry from the ray-tracing and the X-Shooter of the central spectrum, support the contraction + Salpeter IMF. In particular, the Einstein "blue eye" provides evidence of the two-stage IMF scenario (C. Weidner et al. 2013) for the early stage of ETG formation.

Finally, KiDS J0233−3447 represents a reference case for analyses that will combine similar wide wavelength baseline data sets, from optical to NIR, from future surveys from ground and from space.

Acknowledgments

We acknowledge the support from the National Natural Science Foundation of China (Grant No. 12588202). R.L. acknowledges the National Natural Science Foundation of China (No. 12203050), the China Manned Space Program (grant No. CMS-CSST-2025-A03), and the Natural Science Foundation of Henan Province of China (grant No. 242300420235). N.R.N. acknowledges financial support from the Research Fund for International Scholars of the National Science Foundation of China, grant No. 12150710511. R.L. acknowledges the support by National Key R&D Program of China No. 2022YFF0503403, the support of National Natural Science Foundation of China (No 11988101), the support from the Ministry of Science and Technology of China (No. 2020SKA0110100), the science research grants from the China Manned Space Program (No. CMS-CSST-2025-A03), CAS Project for Young Scientists in Basic Research (No. YSBR-062). C.T. acknowledges funding from INAF research grant 2022 LEMON. H.C.F. acknowledges the financial support of the National Natural Science Foundation of China (grant No. 12203096) and Yunnan Fundamental Research Projects (grant No. 202301AT070339). G.D. acknowledges support by UKRI-STFC grants ST/T003081/1 and ST/X001857/1.

Appendix
Multiband Lens Model

In this appendix, we present the details of the multiband lens modeling that we performed to obtain the source-uncontaminated photometry of the lens in eight bands: *griZYJHK*$_s$. We used the same code (LENSED) and method as described in Section 2.2, but we applied them to the KiDS and VIKING images instead of the AO image. We modeled the lens light, source light, and mass distribution with a de Vaucouleurs profile, elliptical Sérsic profile, and SIE profile, respectively. For the *g*-, *r*-, and *i*-band fits, the model had a total of 18 free parameters: 6 for the lens light (x/y center, total magnitude, effective radius, axis ratio, and position angle), 5 for the SIE mass profile (x/y center, Einstein radius, axis ratio, and position angle), and 7 for the source light (x/y center, total magnitude, effective radius, Sérsic index, axis ratio, and position angle). We varied the parameters of these profiles independently in each band. We used the same code as in Section 2.2 to explore the parameter space and obtain the best-fitting models and the uncertainties. For the lower-resolution NIR images, where the light profile parameters are less constrained, we fixed the effective radius and axis ratio of the lens light, as well as the Sérsic index and axis ratio of the source light, to the best-fit values from the AO model. This reduced the number of free parameters in these fits to 14 (4 for lens light, 5 for lens mass, and 5 for source light).

Table A1 summarizes the main parameters obtained from the multiband lens modeling. The total magnitudes of the lens, as well as the effective radii, the axis ratios, and the position angles, are reported in the table. The Einstein radii, axis ratios, and position angles of the mass profiles are also shown. Figure 3 shows the images, the models, and the residuals in each band. The models can reproduce the observed features of the lens system, such as the lensed arcs and the counterimage, with small residuals. The parameters obtained from the multiband lens modeling are consistent with those obtained from the AO model within the uncertainties. Despite leaving the total mass parameters of the lens model free to vary, we have found an incredibly tight distribution of their values over the eight-band models, with $R_{\rm Ein} = 1\farcs28 \pm 0\farcs02$, $(b/a)_{\rm mass} = 0.94 \pm 0.02$, and $\rm PA_{mass} = 148° \pm 9°$, which are fully

Table A1
Parameters of the Multiband Lens Model

Band	*g*	*r*	*i*	*Z*	*Y*	*J*	*H*	K_s
$\rm mag_*$	23.82 ± 0.14	22.75 ± 0.21	22.13 ± 0.33	21.24 ± 0.01	20.68 ± 0.01	20.24 ± 0.01	19.74 ± 0.01	19.13 ± 0.01
$R_{\rm eff*}$ (arcsec)	1.76 ± 0.19	1.57 ± 0.31	0.48 ± 0.32	0.26(fixed)	0.26(fixed)	0.26(fixed)	0.26(fixed)	0.26(fixed)
$(b/a)_*$	0.52 ± 0.21	0.80 ± 0.13	0.64 ± 0.20	0.85(fixed)	0.85(fixed)	0.85(fixed)	0.85(fixed)	0.85(fixed)
$\rm PA_*$ (deg)	78.6 ± 43.9	84.0 ± 42.6	80.6 ± 54.0	85.6 ± 0.7	48.7 ± 1.4	144.8 ± 0.1	76.5 ± 0.5	170.9 ± 0.1
$R_{\rm Ein}$ (arcsec)	1.31 ± 0.07	1.30 ± 0.02	1.28 ± 0.19	1.28 ± 0.01	1.29 ± 0.01	1.30 ± 0.01	1.27 ± 0.01	1.23 ± 0.01
$(b/a)_{\rm mass}$	0.94 ± 0.01	0.95 ± 0.01	0.94 ± 0.02	0.95 ± 0.01	0.92 ± 0.01	0.90 ± 0.01	0.95 ± 0.01	0.97 ± 0.01
$\rm PA_{mass}$ (deg)	148.5 ± 4.5	145.5 ± 1.3	154.5 ± 8.4	140.8 ± 0.1	159.13 ± 0.3	132.26 ± 0.1	142.28 ± 0.1	157.89 ± 0.1
$\rm mag_{sour}$	23.50 ± 0.13	23.81 ± 0.08	22.79 ± 0.22	-5.11 ± 0.01	-4.48 ± 0.02	-5.49 ± 0.01	-5.27 ± 0.01	-6.14 ± 0.01
$R_{\rm eff}$sour (arcsec)	0.18 ± 0.02	0.09 ± 0.07	0.17 ± 0.03	0.07 ± 0.01	0.11 ± 0.01	0.17 ± 0.01	0.15 ± 0.01	0.12 ± 0.01
$n_{\rm sour}$	0.93 ± 0.22	1.18 ± 0.10	1.02 ± 0.32	1.42(fixed)	1.42(fixed)	1.42(fixed)	1.42(fixed)	1.42(fixed)
$(b/a)_{\rm sour}$	0.61 ± 0.07	0.49 ± 0.03	0.84 ± 0.10	0.76(fixed)	0.76(fixed)	0.76(fixed)	0.76(fixed)	0.76(fixed)
$\rm pa_{sour}$ (deg)	29.7 ± 5.7	14.7 ± 2.1	87.5 ± 54.8	30.4 ± 0.5	163.4 ± 1.4	10.2 ± 0.1	116.3 ± 0.1	17.5 ± 0.1

Note. Parameters of the multiband lens modeling. The first four rows list the best-fit parameters for the lens light profile: magnitude ($\rm mag_*$), effective radius ($R_{\rm eff}{}^*$), axis ratio $(b/a)_*$, and position angle ($\rm PA_*$). Rows 5–7 present the mass model parameters: Einstein radius ($R_{\rm Ein}$), axis ratio $(b/a)_{\rm mass}$, and position angle ($\rm PA_{mass}$). The final rows list the parameters for the lensed source: magnitude ($\rm mag_{sour}$), effective radius ($R_{\rm eff}$sour), Sérsic index ($n_{\rm sour}$), axis ratio $(b/a)_{\rm sour}$, and position angle ($\rm pa_{sour}$).

consistent with the AO parameters in Table 1. This indicates that the mass distribution of the lens is robust and stable. The effective radii of the light of the central galaxy show some variation between the *gr* bands and the other bands, which is mainly due to the low signal-to-noise ratio in the *gr* bands.

ORCID iDs

Rui Li https://orcid.org/0000-0002-3490-4089
Nicola R. Napolitano https://orcid.org/0000-0003-0911-8884
Giuseppe D'Ago https://orcid.org/0000-0001-9697-7331
Vyacheslav N. Shalyapin https://orcid.org/0000-0003-3062-7835
Kai Zhu https://orcid.org/0000-0002-2583-2669
Xiaotong Guo https://orcid.org/0000-0002-2338-7709
Chiara Spiniello https://orcid.org/0000-0002-3909-6359
Crescenzo Tortora https://orcid.org/0000-0001-7958-6531
Haicheng Feng https://orcid.org/0000-0002-1530-2680
Zhiqi Huang https://orcid.org/0000-0003-3070-3412
Koen Kuijken https://orcid.org/0000-0002-3827-0175
Linghua, Xie https://orcid.org/0000-0002-2831-8630
Mario Radovich https://orcid.org/0000-0002-3585-866X

References

Auger, M. W., Treu, T., Bolton, A. S., et al. 2009, ApJ, 705, 1099
Barbosa, C. E., Spiniello, C., Arnaboldi, M., et al. 2021, A&A, 645, L1
Barnabè, M., Czoske, O., Koopmans, L. V. E., Treu, T., & Bolton, A. S. 2011, MNRAS, 415, 2215
Barone-Nugent, R. L., Sonnenfeld, A., Wyithe, J. S. B., et al. 2015, MNRAS, 453, 3068
Bellstedt, S., Forbes, D. A., Romanowsky, A. J., et al. 2018, MNRAS, 476, 4543
Binney, J., & Tremaine, S. 1987, Galactic Dynamics (Princeton, NJ: Princeton Univ. Press)
Bolton, A. S., Brownstein, J. R., Kochanek, C. S., et al. 2012, ApJ, 757, 82
Bolton, A. S., Burles, S., Koopmans, L. V. E., et al. 2008, ApJ, 682, 964
Bruzual, G., & Charlot, S. 2003, MNRAS, 344, 1000
Cañameras, R., Nesvadba, N. P. H., Kneissl, R., et al. 2017, A&A, 600, L3
Cappellari, M. 2017, MNRAS, 466, 798
Cappellari, M., McDermid, R. M., Alatalo, K., et al. 2012, Natur, 484, 485
Ciesla, L., Béthermin, M., Daddi, E., et al. 2020, A&A, 635, A27
Conroy, C., & van Dokkum, P. G. 2012, ApJ, 760, 71
de Jong, J. T. A., Verdoes Kleijn, G. A., Kuijken, K. H., & Valentijn, E. A. 2013, ExA, 35, 25
de Vaucouleurs, G. 1948, AnAp, 11, 247
Dehnen, W., & McLaughlin, D. E. 2005, MNRAS, 363, 1057
Dubois, Y., Gavazzi, R., Peirani, S., & Silk, J. 2013, MNRAS, 433, 3297
Duffy, A. R., Schaye, J., Kay, S. T., et al. 2010, MNRAS, 405, 2161
Dutton, A. A., & Treu, T. 2014, MNRAS, 438, 3594
Edge, A., Sutherland, W., Kuijken, K., et al. 2013, Msngr, 154, 32
Etherington, A., Nightingale, J. W., Massey, R., et al. 2023, MNRAS, 521, 6005
Fulton, E., & Barnes, J. E. 2001, Ap&SS, 276, 851
Gnedin, O. Y., Kravtsov, A. V., Klypin, A. A., & Nagai, D. 2004, ApJ, 616, 16
Graham, A. W., Merritt, D., Moore, B., Diemand, J., & Terzić, B. 2006, AJ, 132, 2701
Greggio, L., & Renzini, A. 2012, arXiv:1203.1221
He, K., Zhang, X., Ren, S., & Sun, J. 2016, in 2016 IEEE Conf. on Computer Vision and Pattern Recognition (Piscataway, NJ: IEEE), 770
He, Q., Li, H., Li, R., et al. 2020, MNRAS, 496, 4717
Humphrey, P. J., & Buote, D. A. 2006, ApJ, 639, 136
Ivezić, Ž., Kahn, S. M., Tyson, J. A., et al. 2019, ApJ, 873, 111
Johansson, P. H., Naab, T., & Ostriker, J. P. 2012, ApJ, 754, 115
Kazantzidis, S., Zentner, A. R., & Kravtsov, A. V. 2006, ApJ, 641, 647
Komatsu, E., Smith, K. M., Dunkley, J., et al. 2011, ApJS, 192, 18
Koopmans, L. V. E., Bolton, A., Treu, T., et al. 2009, ApJL, 703, L51
Koopmans, L. V. E., & Treu, T. 2002, ApJL, 568, L5
Koopmans, L. V. E., Treu, T., Bolton, A. S., Burles, S., & Moustakas, L. A. 2006, ApJ, 649, 599
Kormann, R., Schneider, P., & Bartelmann, M. 1994, A&A, 284, 285
La Barbera, F., Ferreras, I., Vazdekis, A., et al. 2013, MNRAS, 433, 3017
Laureijs, R., Amiaux, J., Arduini, S., et al. 2011, arXiv:1110.3193
Li, H., Ge, J., Mao, S., et al. 2017, ApJ, 838, 77
Li, R., Napolitano, N. R., Spiniello, C., et al. 2021, ApJ, 923, 16
Li, R., Shu, Y., & Wang, J. 2018, MNRAS, 480, 431
Li, S., Li, R., Zhu, K., et al. 2024, MNRAS, 529, 4633
Lu, S., Zhu, K., Cappellari, M., et al. 2024, MNRAS, 530, 4474
Martín-Navarro, I., de Lorenzo-Cáceres, A., Gadotti, D. A., et al. 2024, A&A, 684, 15
Martín-Navarro, I., Vazdekis, A., La Barbera, F., et al. 2015, ApJL, 806, L31
Mendel, J. T., Beifiori, A., Saglia, R. P., et al. 2020, ApJ, 899, 87
Merritt, D. 1985, AJ, 90, 1027
Napolitano, N. R., Romanowsky, A. J., & Tortora, C. 2010, MNRAS, 405, 2351
Navarro, J. F., Frenk, C. S., & White, S. D. M. 1997, ApJ, 490, 493
Nipoti, C., Treu, T., & Bolton, A. S. 2009, ApJ, 703, 1531
Oser, L., Ostriker, J. P., Naab, T., Johansson, P. H., & Burkert, A. 2010, ApJ, 725, 2312
Osipkov, L. P. 1979, PAZh, 5, 77
Remus, R.-S., Dolag, K., Naab, T., et al. 2017, MNRAS, 464, 3742
Ruff, A. J., Gavazzi, R., Marshall, P. J., et al. 2011, ApJ, 727, 96
Schwab, J., Bolton, A. S., & Rappaport, S. A. 2010, ApJ, 708, 750
Sellwood, J. A., & McGaugh, S. S. 2005, ApJ, 634, 70
Sérsic, J. L. 1963, BAAA, 6, 41
Shajib, A. J., Treu, T., Birrer, S., & Sonnenfeld, A. 2021, MNRAS, 503, 2380
Shetty, S., & Cappellari, M. 2014, ApJL, 786, L10
Shu, Y., Bolton, A. S., Kochanek, C. S., et al. 2016a, ApJ, 824, 86
Shu, Y., Bolton, A. S., Mao, S., et al. 2016b, ApJ, 833, 264
Sonnenfeld, A. 2024, A&A, 690, A325
Sonnenfeld, A., Gavazzi, R., Suyu, S. H., Treu, T., & Marshall, P. J. 2013a, ApJ, 777, 97
Sonnenfeld, A., Nipoti, C., & Treu, T. 2014, ApJ, 786, 89
Sonnenfeld, A., Treu, T., Gavazzi, R., et al. 2012, ApJ, 752, 163
Sonnenfeld, A., Treu, T., Gavazzi, R., et al. 2013b, ApJ, 777, 98
Sonnenfeld, A., Treu, T., Marshall, P. J., et al. 2015, ApJ, 800, 94
Spergel, D., Gehrels, N., Baltay, C., et al. 2015, arXiv:1503.03757
Spiniello, C., Koopmans, L. V. E., Trager, S. C., Czoske, O., & Treu, T. 2011, MNRAS, 417, 3000
Spiniello, C., Sergeyev, A. V., Marchetti, L., et al. 2019, MNRAS, 485, 5086
Spiniello, C., Trager, S., Koopmans, L. V. E., & Conroy, C. 2014, MNRAS, 438, 1483
Stein, G., Blaum, J., Harrington, P., Medan, T., & Lukić, Z. 2022, ApJ, 932, 107
Tan, C. Y., Shajib, A. J., Birrer, S., et al. 2024, MNRAS, 530, 1474
Tessore, N., Bellagamba, F., & Metcalf, R. B. 2016, MNRAS, 463, 3115
Thomas, J., Saglia, R. P., Bender, R., et al. 2007, MNRAS, 382, 657
Tortora, C., Hunt, L. K., & Ginolfi, M. 2022, A&A, 657, A19
Tortora, C., La Barbera, F., Napolitano, N. R., et al. 2014, MNRAS, 445, 115
Tortora, C., La Barbera, F., Napolitano, N. R., et al. 2016, in The Universe of Digital Sky Surveys, ed. N. R. Napolitano et al. Vol. 42 (Berlin: Springer), 215
Tortora, C., Napolitano, N. R., Romanowsky, A. J., & Jetzer, P. 2010, ApJL, 721, L1
Tortora, C., Romanowsky, A. J., & Napolitano, N. R. 2013, ApJ, 765, 8
Treu, T., Auger, M. W., Koopmans, L. V. E., et al. 2010, ApJ, 709, 1195
Treu, T., Dutton, A. A., Auger, M. W., et al. 2011, MNRAS, 417, 1601
Treu, T., Koopmans, L. V., Bolton, A. S., Burles, S., & Moustakas, L. A. 2006, ApJ, 640, 662
Treu, T., & Koopmans, L. V. E. 2002, ApJ, 575, 87
Treu, T., & Koopmans, L. V. E. 2004, ApJ, 611, 739
van Dokkum, P., Brammer, G., Wang, B., Leja, J., & Conroy, C. 2024, NatAs, 8, 119
Wang, C., Li, R., Zhu, K., et al. 2024, MNRAS, 527, 1580
Wang, Y., Vogelsberger, M., Xu, D., et al. 2019, MNRAS, 490, 5722
Weidner, C., Ferreras, I., Vazdekis, A., & La Barbera, F. 2013, MNRAS, 435, 2274
Wong, K. C., Tran, K.-V. H., Suyu, S. H., et al. 2014, ApJL, 789, L31
Wright, A. H., Kuijken, K., Hildebrandt, H., et al. 2024, A&A, 686, A170
Xu, D., Springel, V., Sluse, D., et al. 2017, MNRAS, 469, 1824
Zhan, H. 2011, Sci. Sin. Phys. Mech. Astron., 41, 1441
Zhu, K., Lu, S., Cappellari, M., et al. 2023, MNRAS, 522, 6326
Zhu, K., Lu, S., Cappellari, M., et al. 2024, MNRAS, 527, 706